Supplementary Material

The Surface and Catalytic Chemistry of the First Row Transition Metal Phosphides in Deoxygenation

Yang He and Siris Laursen[*]

Department of Chemical and Bimolecular Engineering, University of Tennessee, Knoxville

E-mail: slaursen@utk.edu

---

[*]To whom correspondence should be addressed

Content

Calculation details continued

Preliminary experimental results on surface composition change of TiP

Figure S1. Calculated surface energies for the promising facets over the 1st row TM phosphides

Figure S2. Model figures for the slabs used for the calculations of hydrogen and oxygen dissociation

Figure S3. Model figures for the slabs used for the calculations of ethylene adsorption and phenol deoxygenation towards benzene

Figure S4. Model figures for the distance between two adjacent adsorbed H atoms over the 1st row TM phosphides

Figure S5. Model figures for the distance between two adjacent intermediates of phenol deoxygenation over the 1st row TM phosphides

Figure S6. Gibb's free energy of phosphorus removal from P-rich to stoichiometric to P-lean surfaces to determine the termination of the 1st row TM phosphides

Figure S7. Energetically unfavorable surface reaction sites for phenol adsorption over CrP, Fe_2P, Co_2P, and Ni_2P

Figure S8. Phenol deoxygenation reaction mechanism over the 1st row TM phosphides via the direct reaction pathway

Figure S9. Phenol deoxygenation reaction mechanism over the 1st row TM phosphides via the reaction pathway of indirect-a

Figure S10. Phenol deoxygenation reaction mechanism over the 1st row TM phosphides via the reaction pathway of indirect-b

Figure S11. Phenol deoxygenation reaction mechanism over the 1st row TM phosphides via the reaction pathway of indirect-c

Figure S12. Phenol deoxygenation reaction mechanism over the 1st row TM phosphides via the tautomerization reaction pathway

pathways over the 1st row TM phosphides

Table S5. Thermodynamic energetics for H_2O formation and desorption steps over the 1st row TM phosphides

Table S6. Bader charge analysis of intermediate in dehydroxylation step

Table S7. Bader charge analysis of the surface of 1st row TM phosphides

Table S8. Bond lengths between intermediate and surface in each reaction step

Table S9. Bond lengths of transition state over the 1st row TM phosphides

1 Calculation details continued

1.1 Probe Molecule Selection for Correlations

Oxygen dissociative adsorption energy was used as a marker to estimate the surface reactivity toward oxygen. Because of the magnetic electronic structure of O_2, O–O bonding is not well captured in DFT. Therefore, it is critical to adjust calculated dissociative adsorption energies for O_2 using the experimentally determined bond dissociation energy as a reference. Within our calculation framework of using PBE-sol, O_2 dissociation is 3.4 eV/atom, which is 0.8 eV/atom higher than the experimentally measured value (2.6 eV per oxygen atom[1]). The calculated O_2 dissociative adsorption energies over the 1st row TM phosphides in Figure S20 and Figure S21 in the Supporting Information have been corrected by this energy difference to give a more realistic view of the energies. Ethylene was chosen as a general marker for carbon affinity to partially circumvent the effect of aromatic stabilization and geometry of benzene. Because of these factors, benzene adsorption is inherently limited over several of the TM phosphides. These effects may cause benzene to underestimate surface carbon affinity if were used as a reactivity probe. Because of the generality of using ethylene as a probe, transferability of our results to other studies and materials is enhanced. Dissociative adsorption of H_2 was also used as a marker for the surface chemistry towards atomic H. The

adsorption energy is calculated as eqn (1).

$$\Delta E_{ads} = E_{total} - E_{slab} - E_{gas} \tag{1}$$

1.2 Magnetic Properties Calculations

It is critical to properly estimate the magnetic properties for the 1st row TM phosphides to capture their electronic structure and surface chemistry. The magnetic moment of the 1st row TM phosphides was determined by testing a wide range of magnetic moments until an energetic minimum was identified while optimizing the bulk solids. Fe_2P and CrP were calculated as paramagnetic with magnetic moments of 1.36 and 0.53 μ_B for Fe and Cr, respectively. In both cases, when the calculations included atomic adsorbates (H and O) as well as large fragments or molecules (phenyl, bidentate benzyne, phenol, etc.), magnetic moments on metals were favorable. Nickel in Ni_2P exhibited residual magnetic moments of 0.1-0.2 μ_B. With large fragments or molecules presented on surface (phenyl, bidentate benzynephenol, etc.), the magnitude of magnetic moment of Ni diminished to zero. For TiP, VP, and Co_2P, no magnetic moments were observed to be favorable under any condition.

1.3 Structural Aspects of the Modeling

The 1st row TM phosphides were modeled as infinite slabs using periodic boundary conditions. Surface unit cells were constructed by at least 2−3 stoichiometric layers (at least 6 atomic layers) with a periodicity of 2x2 or 3x3, which allows the surface coverage of adsorbates as low as 1/9 ML. This slab geometry lead to a fully developed TM phosphide electronic structure in comparison to the bulk. A vacuum space of 20 $\mathring{A}$ was implemented with a dipole correction added in the free space to eliminate the interaction between slabs. The top two layers and surface intermediates were allowed to optimize, and the remainder of the elements in the slab were fixed to their optimized bulk configuration. The kinetic barriers for elementary reaction steps were calculated using climbing nudged elastic band (cNEB) approach or the DIMER method.[2–6] The models were optimized when forces were

achieved to be less than 0.1 eV/Ang on each atom. The INCAR files utilized for the cNEB and DIMER method were provided at the end of the Supporting Information document.

1.4 Surface Facet Determination

The selection of surface facet for each of the 1st row TM phosphides followed established theoretical studies or were isolated manually. The most favorable surface facets of Ni_2P (001) was chosen from established studies.[7,8] When surface facets were selected manually, the surface facets with the highest degree of atom packing symmetry, lowest like-ion ion-ion interactions, and the lowest degree of surface corrugation were chosen. The surface energies for the promising facets were then calculated and compared to find the lowest energy facet for use in the study. The surfaces of TiP(001), VP(001), CrP(101), Fe_2P(100), and Co_2P(010) were found to be the most energetically favorable facets (see Figure S1 in the Supporting Information).

1.5 Surface Termination Determination

An *ab initio* thermodynamics approach was utilized to determine the surface termination of the TM phosphides under a reaction condition of 300°C and ∼70 mol% H_2 at 1.0 atm. The aim of this approach was to model the surface composition of the TM phosphides in their condition after being exposed and modified by the reducing H_2 environment. The approach includes a reaction between atomic H from H_2 and surface phosphorous that results in the formation of PH_3. Through this reaction, weakly bound surface phosphorous may be removed until it stability produces an endothermic energetic for its removal. Again, the approach models the surface of the materials when in contact with reducing reaction conditions and not the state encountered during synthesis conditions where the chemical potential of phosphorus would likely be high or difficult to model, e.g., in the use of PH3, white or yellow phosphorus, or phosphate/ite ligands within an organometallic precursor.[9–12] The approach utilized a range of manually-produced P-rich to P-lean surfaces. Where the

thermodynamics of sequentially removing surface phosphorus atoms crossed from exothermic to endothermic was used to mark when the surface composition became stable. The equations used for the calculations are:

$$\Delta G(T,P) = G_f + N_{PH_3}\mu_{PH_3} - (G_i + N_{H_2}\mu_{H_2}) \tag{2}$$

G_i and G_f are the Gibb's free energy of the TM phosphides slab before and after each phosphorus atom removal, respectively, which can be presented as

$$G = E + E_{vib} + PV - TS \tag{3}$$

where N_X is the number of molecules of reactant and product used and produced in the reaction. The internal and vibrational energy of the systems are represented by E and E_{vib}. The chemical potential of phosphine and molecular H_2 are represented by μ_{PH_3} and μ_{H_2}. The gas phase chemical potentials (μ) are computed using the following expression.

$$\mu = \Delta\mu_X(T, P) + E_X \tag{4}$$

The internal energy, E_X, is from DFT calculations, while the temperature and pressure effects on the free energy of the gas phase molecules was obtained from NIST thermochemical tables.[13] Combining eqn (2)-(4) to obtain eqn (5).

$$\Delta G(T,P) = (E_f + \Delta\mu_{PH_3}(T,P) + E_{PH_3} + E_{vib,f}) - (E_I + 1.5\Delta\mu_{H_2}(T,P) + E_{H_2} + E_{vib,i}) \tag{5}$$

Considering the common flow reactor regime and the fact that any PH_3 produced would be swept away from the catalyst, the chemical potential of PH_3 can be assumed to be negligible. This simplifies the calculation such that it is only dependent upon the formation energy of PH_3 and the chemical potential of H_2. The contribution of surface vibration of initial and final state is also commonly neglected since their contributions are marginal in comparison to reaction energetics and gas phase chemical potentials. Therefore, eqn (5) can be simplified to eqn (6).

$$\Delta G(T,P) \approx E_f + E_{PH_3} - E_I - 1.5\Delta\mu_{H_2}(T,P) - E_{H_2} \tag{6}$$

1.6 Kinetic Rate Constant Calculation

To shed light upon the active reaction pathways and the rate-determining steps within the active mechanism, the reaction rate constants were determined utilizing the Eyring equation:

$$\text{k} = \frac{k_B T}{h} \frac{Q_{TS,vib}}{Q_{IS,vib}} \text{e}^{\frac{-E_a}{k_B T}} \tag{7}$$

where k_b is the Boltzmann constant, T is the temperature, h is Plank's constant, $Q_{TS,vib}$ and $Q_{IS,vib}$ are the partition functions for the transition state and the initial state, respectively, and E_a is the activation energy calculated from DFT. Q_{vib} is calculated as:

$$Q_{vib} = \prod_i \frac{1}{1 - e^{\frac{-h v_i}{k_B T}}} \tag{8}$$

where v_i is the vibrational frequency of each vibrational mode of the adsorbates computed from DFT calculations. The reaction conditions were set to 300°C with 70% H_2.

2 Preliminary experimental results on surface composition change of TiP

Guaiacol deoxygenation reaction was performed over TiP and Ni_2P in the temperature range of 200 to 700°C in a gas flow reactor with a catalyst loading of 500 mg for TiP (3.0 m^2/g) and 100 mg for Ni_2P (22 m^2/g). Overall gas flow rate of 100 SCCM with 10% H_2 was used. Guaiacol was introduced using a fine-flow rate syringe pump. Effluent of the reactor was analyzed via online sampling with a GC equipped with FID and TCD detectors. Catalyst composition change of Ni_2P and TiP were analyzed by TEM after reaction of 10 hours up to 700°C with elemental mapping via EDS. TiP was found to oxidize even under the reducing environment due to the thermodynamic driving force for Ti oxidation (the oxygen healing energy is –4 eV exothermic). On the other hand, no clear oxidation or phosphorus loss were observed over Ni_2P, which coincided with our calculations.
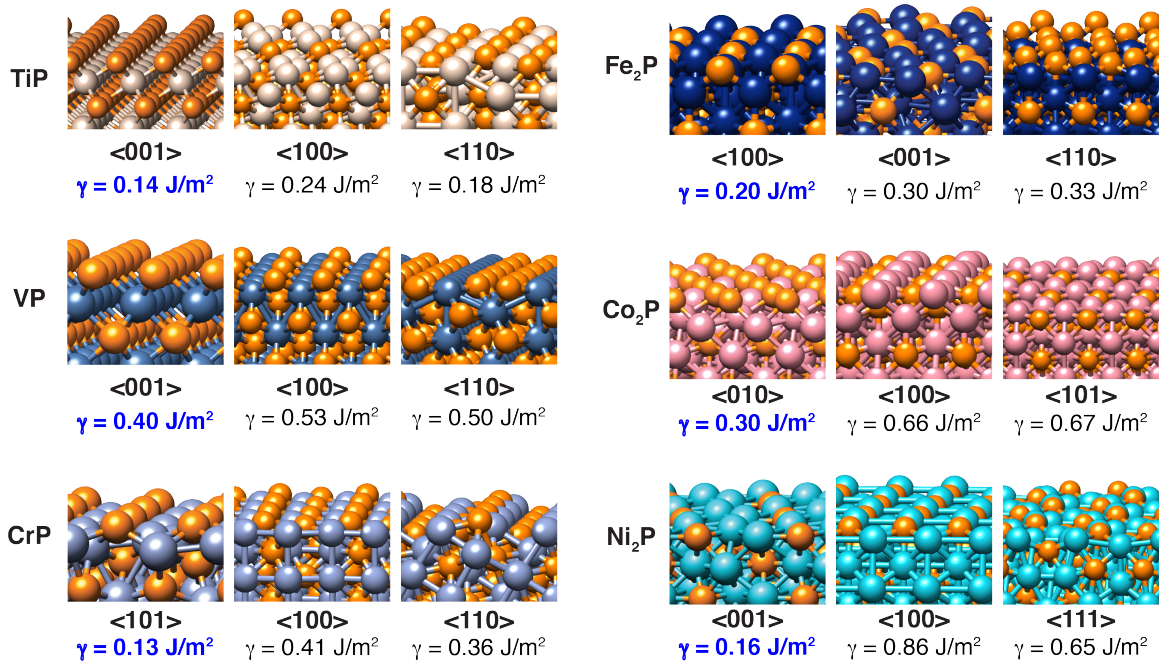
TiP
<001> — $\gamma = 0.14\ J/m^2$
<100> — $\gamma = 0.24\ J/m^2$
<110> — $\gamma = 0.18\ J/m^2$

Fe_2P
<100> — $\gamma = 0.20\ J/m^2$
<001> — $\gamma = 0.30\ J/m^2$
<110> — $\gamma = 0.33\ J/m^2$

VP
<001> — $\gamma = 0.40\ J/m^2$
<100> — $\gamma = 0.53\ J/m^2$
<110> — $\gamma = 0.50\ J/m^2$

Co_2P
<010> — $\gamma = 0.30\ J/m^2$
<100> — $\gamma = 0.66\ J/m^2$
<101> — $\gamma = 0.67\ J/m^2$

CrP
<101> — $\gamma = 0.13\ J/m^2$
<100> — $\gamma = 0.41\ J/m^2$
<110> — $\gamma = 0.36\ J/m^2$

Ni_2P
<001> — $\gamma = 0.16\ J/m^2$
<100> — $\gamma = 0.86\ J/m^2$
<111> — $\gamma = 0.65\ J/m^2$

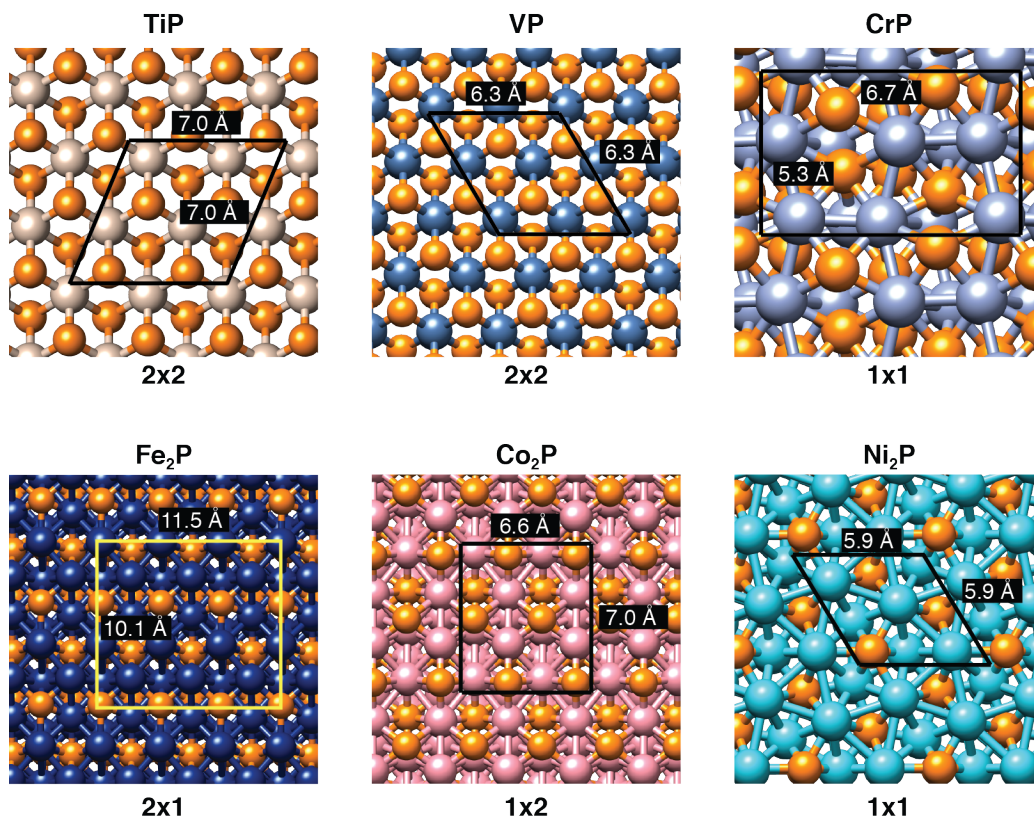**Figure S1:** Model figures for the most favorable facets of the 1st row TM phosphides.

Figure S2: Model figures showing the size of the slabs used for the calculations of hydrogen and oxygen dissociative adsorption. Elements in the model figures are color coded: Ti (light brown), V (medium blue), Cr (light purple), Fe (dark blue), Co (pink), Ni (turquoise), and P (orange).
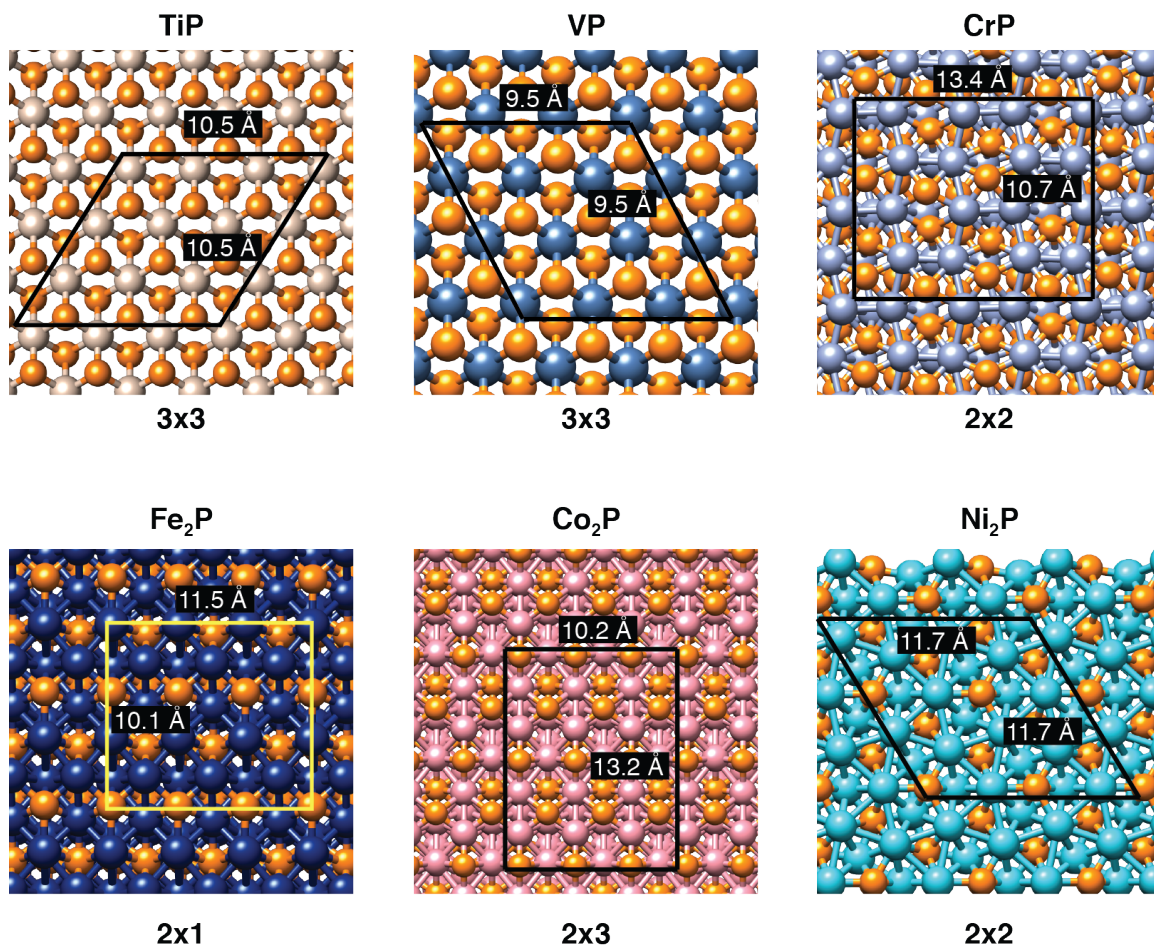
Figure S3: Model figures showing the size of the slabs used for the calculation of phenol transformation towards benzene. Elements in the model figures are color coded: Ti (light brown), V (medium blue), Cr (light purple), Fe (dark blue), Co (pink), Ni (turquoise), and P (orange).
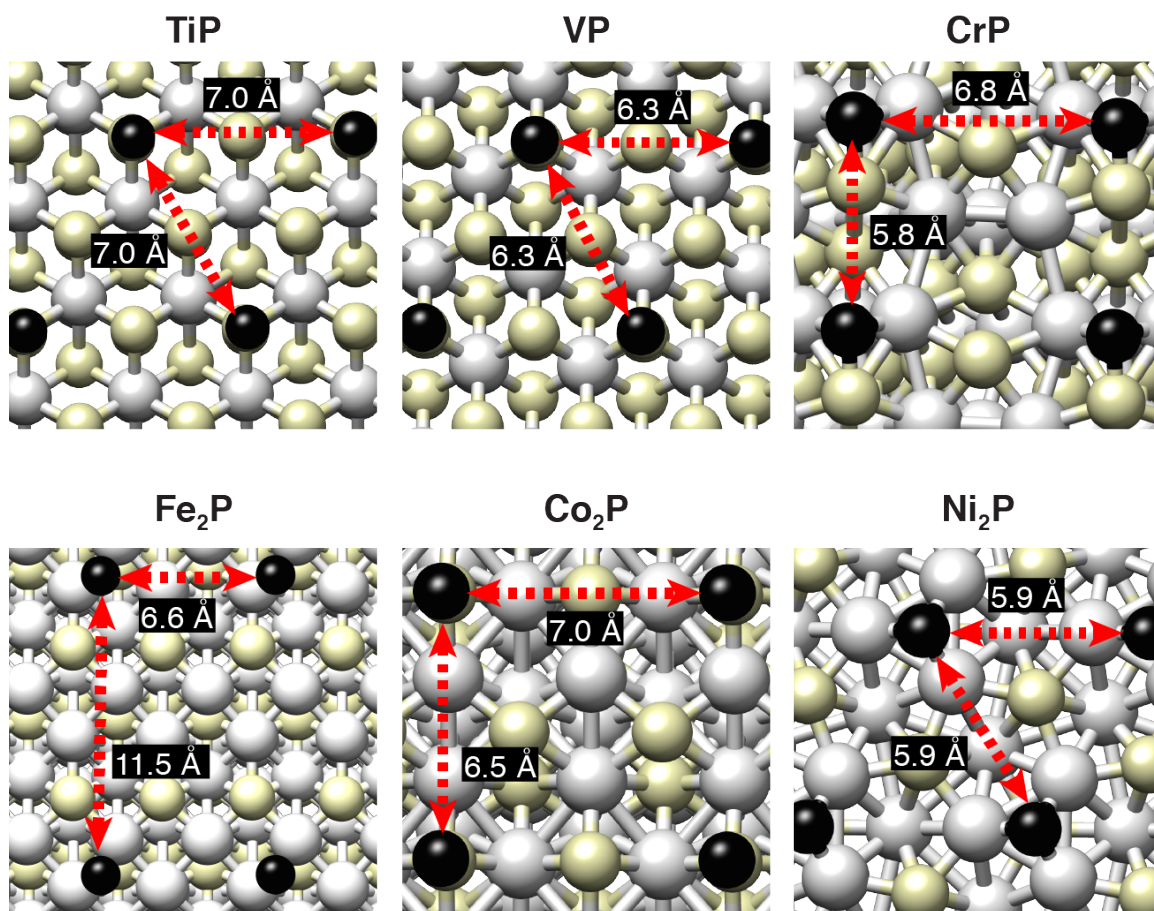
Figure S4: The distance between adsorbates (H or O) is sufficiently long to avoid the effect of lateral interaction on the adsorption energy. Elements in the model figures are color coded: metal (grey), phosphorus (light yellow), carbon (green), and H(black).
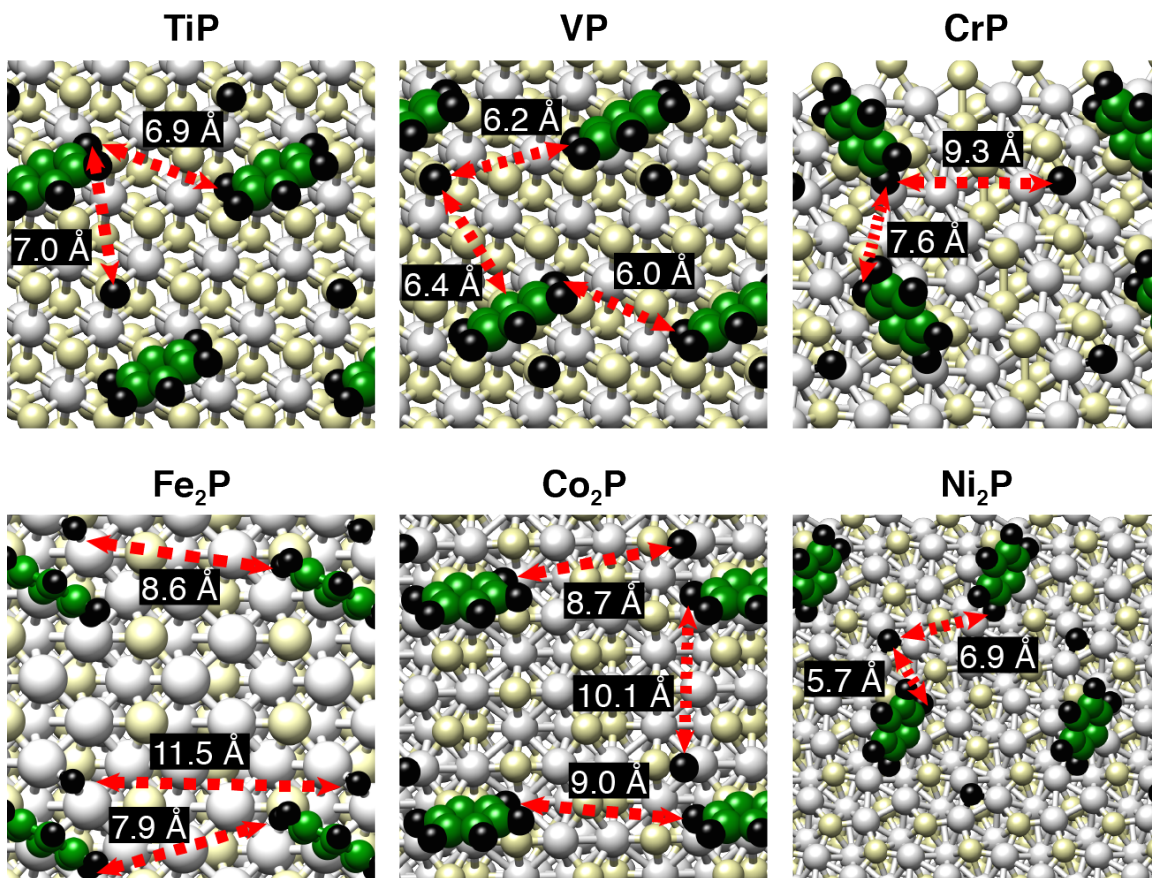
Figure S5: The distance between adsorbates in the hydrogenation reaction step as an example to show that the effect of lateral interaction on reaction step energetics is minimal. Similar results were encountered in other reaction steps and ethylene adsorption. Elements in the model figures are color coded: metal (grey), phosphorus (light yellow), carbon (green), and H(black).
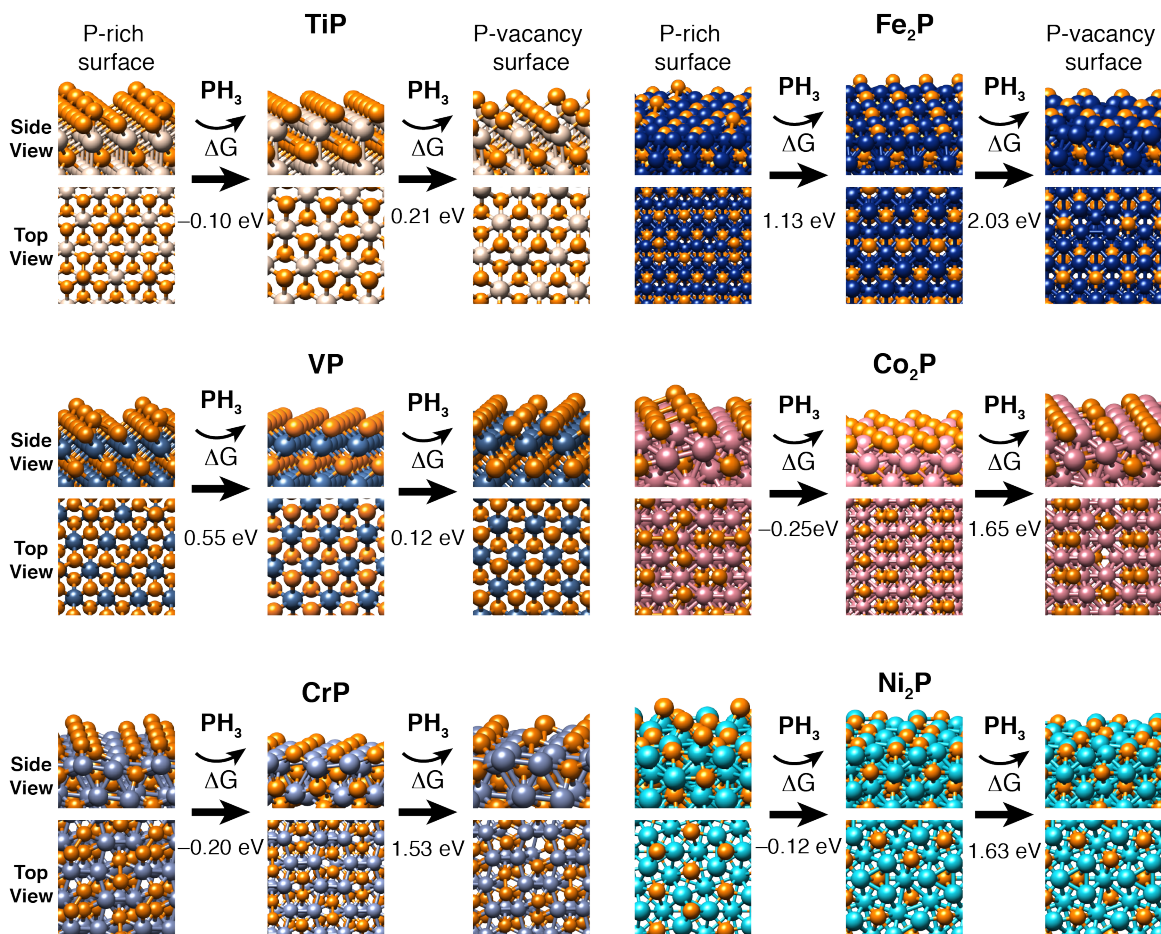
Figure S6: Surface termination determined by calculating the Gibb's free energy of phosphorus removal from P-rich to "as-prepared" to P-lean surface under the reaction conditions of 300°C and approx. 70 mol% H_2 at 1.0 atm. Elements in the model figures are color coded: Ti (light brown), V (medium blue), Cr (light purple), Fe (dark blue), Co (pink), Ni (turquoise), P (orange), C (green), and H (black).
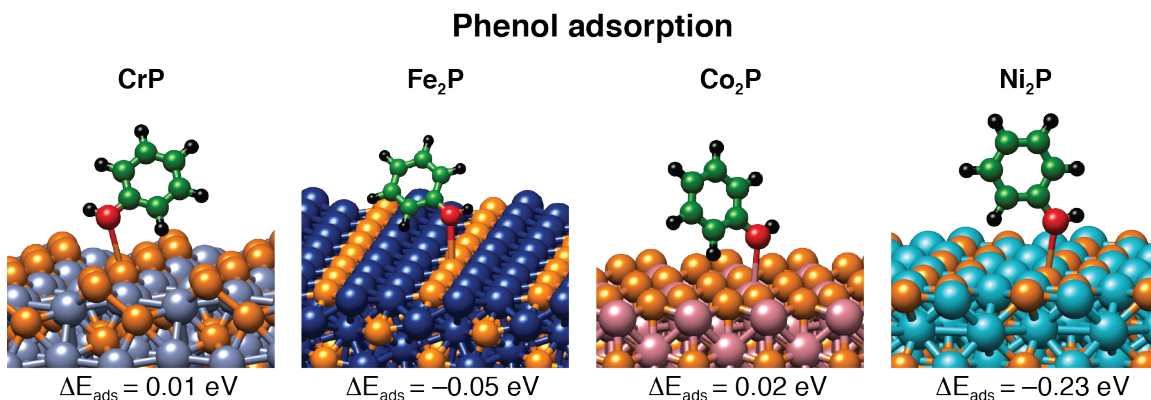
Phenol adsorption

CrP **Fe₂P** **Co₂P** **Ni₂P**

$\Delta E_{ads} = 0.01$ eV $\quad$ $\Delta E_{ads} = -0.05$ eV $\quad$ $\Delta E_{ads} = 0.02$ eV $\quad$ $\Delta E_{ads} = -0.23$ eV

Figure S7: Model figures for other possible surface reaction sites that are less favorable in phenol adsorption over CrP, Fe₂P, Co₂P, and Ni₂P. Adsorption over TiP and VP was completely limited to surface phosphorous sites due to geometric blocking of the metal sites. Other adsorption geometries were also investigated but all relaxed to the adsorption sites presented.
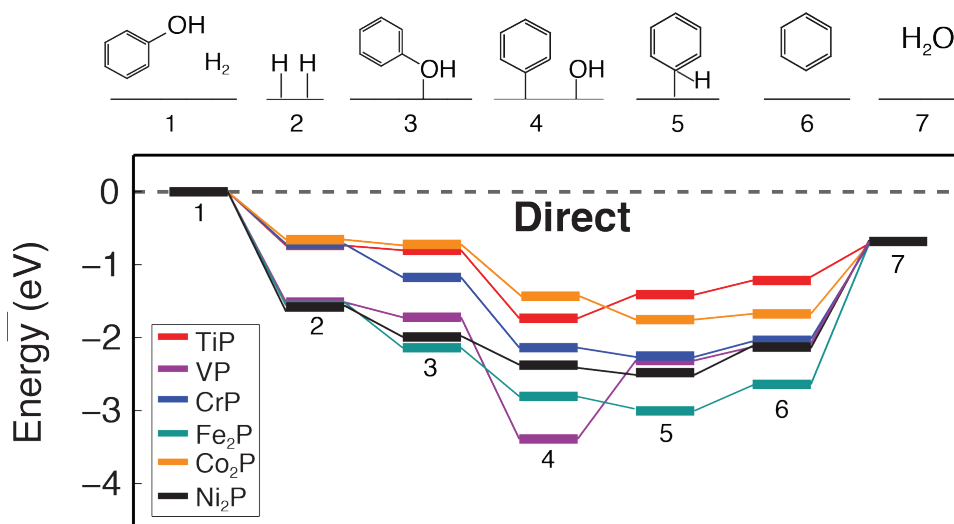

Figure S8: Direct reaction pathway of phenol deoxygenation over the 1_{st} row TM phosphides. The results suggested that the direct reaction pathway is energetically more favorable than any other indirect reaction pathway.
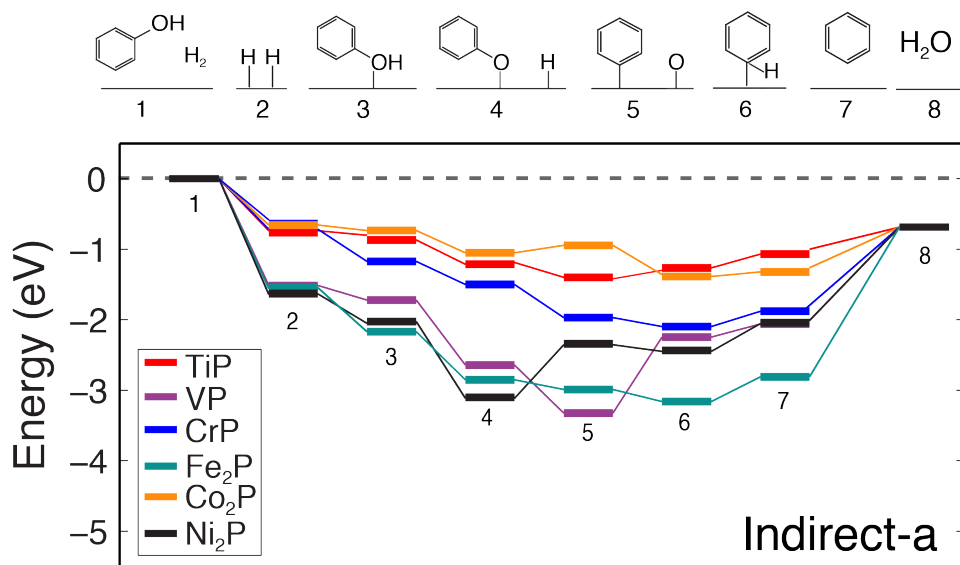
Figure S9: Indirect reaction pathway-a (Indirect-a) of phenol deoxygenation over the 1st row TM phosphides. The thermodynamic driving force for the oxygen removal step was reduced significantly in comparison to the direct reaction pathway.
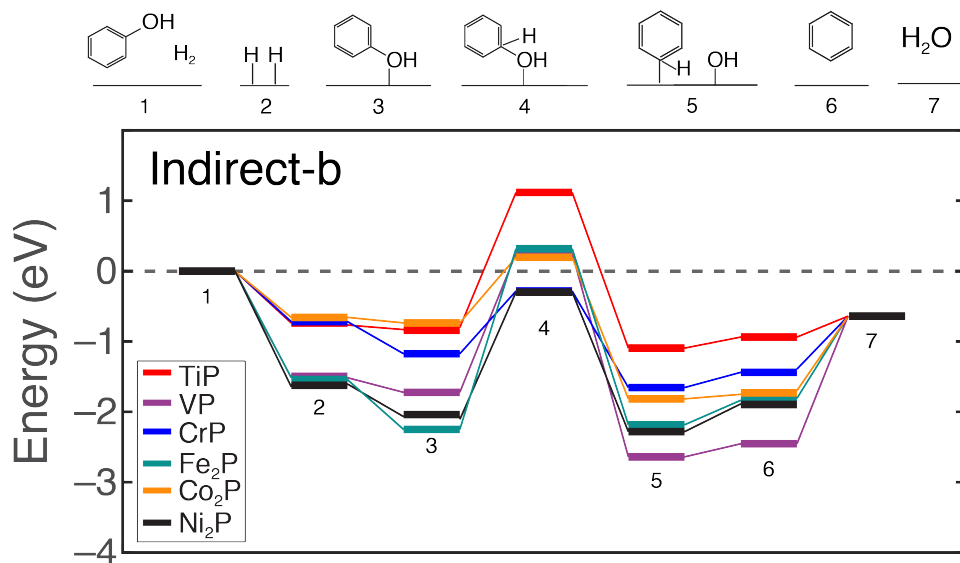

Figure S10: Indirect reaction pathway-b (Indirect-b) of phenol deoxygenation over the 1st row TM phosphides. The highly endothermic energetics for the ring hydrogenation step before oxygen removal indicated it was an energetically unfavorable reaction pathway.
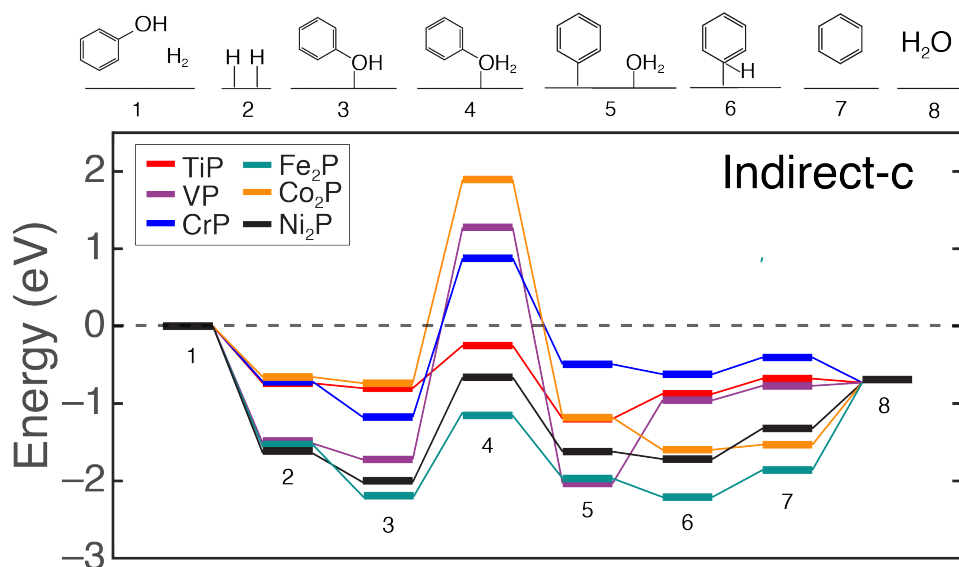
Figure S11: Indirect reaction pathway-c (Indirect-c) of phenol deoxygenation over the 1st row TM phosphides. The highly endothermic energetics for the hydrogenation of the –OH group before C–O cleavage suggested it was not the most energetically favorable reaction pathway.
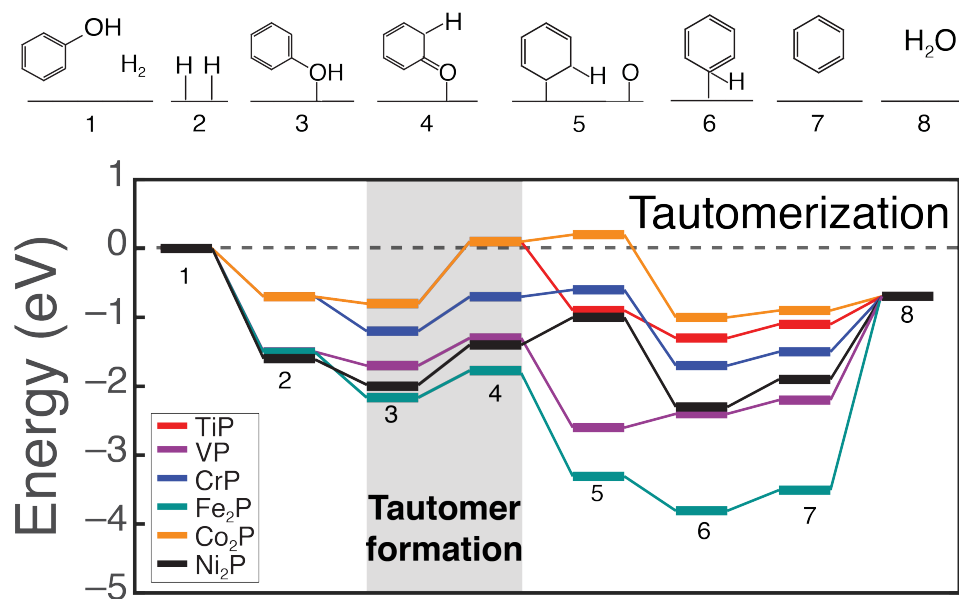

Figure S12: Thermodynamics for the tautomerization of phenol process over the 1st row TM phosphides. The endothermic energetics for the tautomerization step suggested that it was an energetically unfavorable reaction pathway.
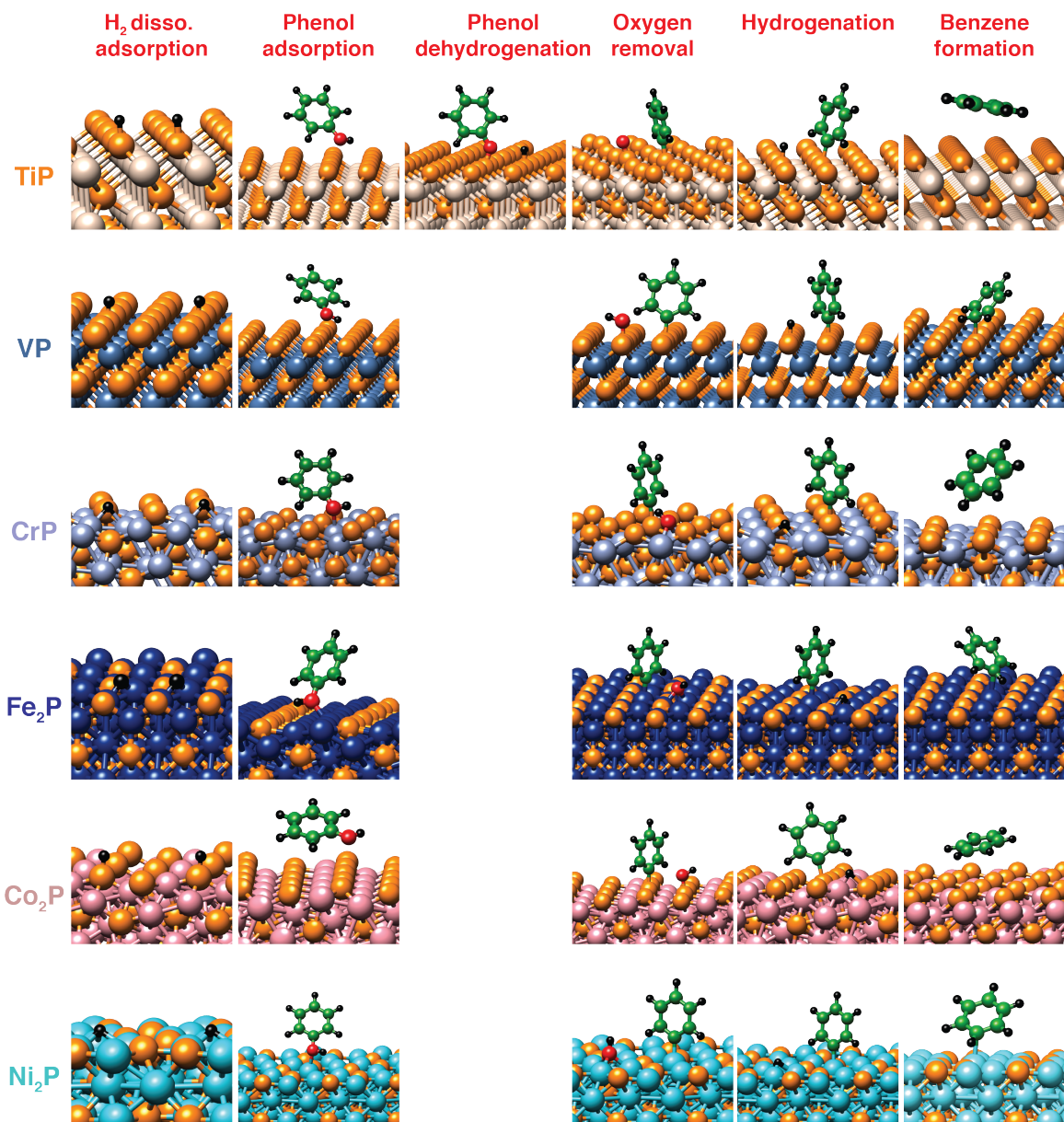
Figure S13: Model figures of the most favorable reaction pathway for phenol deoxygenation over the 1st row TM phosphides.

Figure S14: Model figures for other possible surface reaction sites that are less favorable in phenol deoxygenation reaction steps over CrP, Fe$_2$P, Co$_2$P, and Ni$_2$P. Adsorption over TiP and VP was completely limited to surface phosphorous sites due to geometric blocking of the metal sites. Other adsorption geometries were also investigated but all relaxed to the adsorption sites presented.

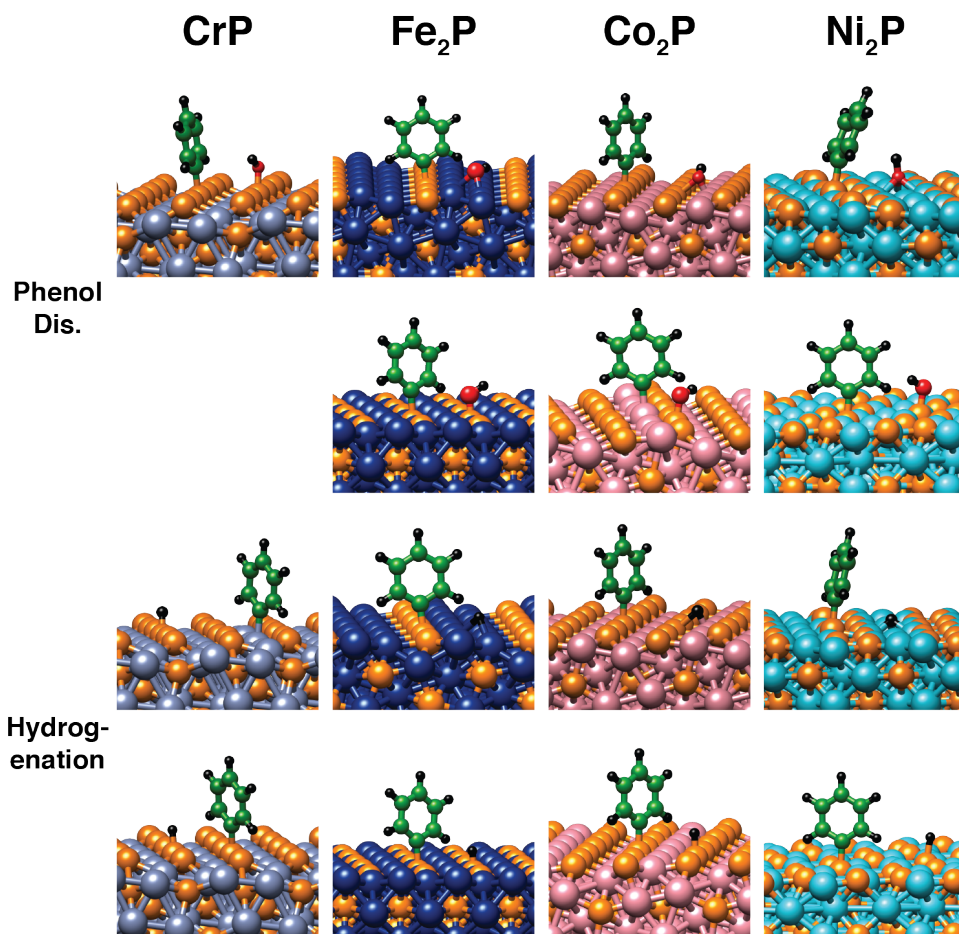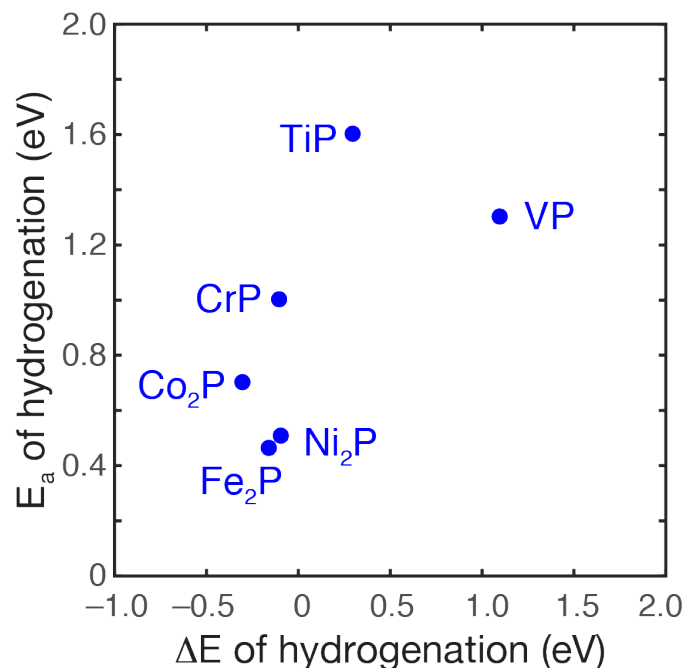**Figure S15:** BEP-like correlation between kinetics and thermodynamics of the hydrogenation step over the 1_{st} row TM phosphides. No clear correlation was found due to hydrogenation being affected significantly by the electronic structure of the phosphides, e.g., limited vs. hydrogenation over metals.

Figure S16: A comparison of phenol deoxygenation reaction via horizontal and vertical orientation over Fe_2P and Ni_2P. The highly endothermic energetics for the hydrogenation steps would likely result in a catalytically inactive surface because of poisoning.
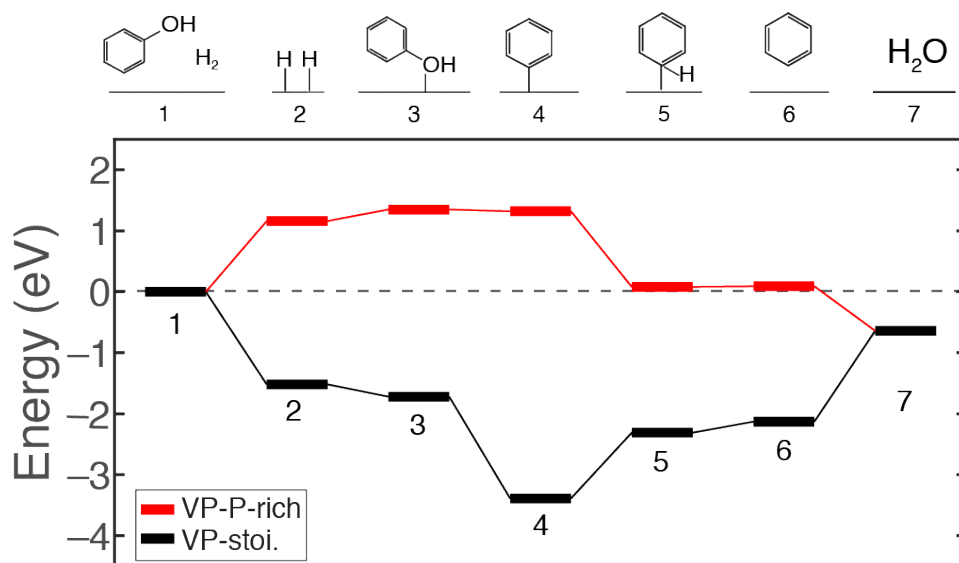
Figure S17: Direct reaction pathway of phenol deoxygenation on P-rich and stoichiometric surface of VP. The aggressive reduction of the ability to dissociate hydrogen and to cleave C–O bond over P-rich VP surface indicated that the surface was less favorable for phenol deoxygenation than the "as-prepared" VP surface.
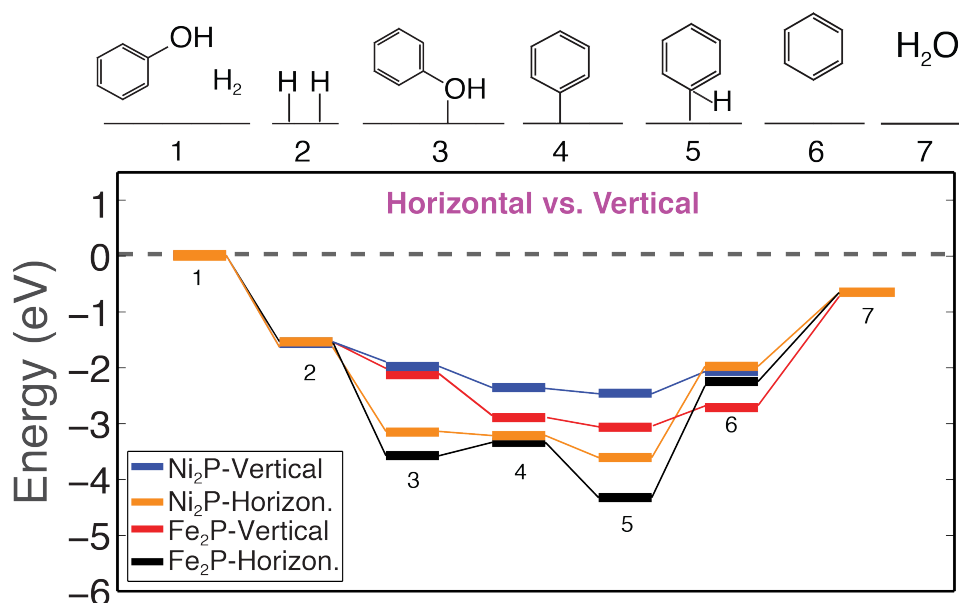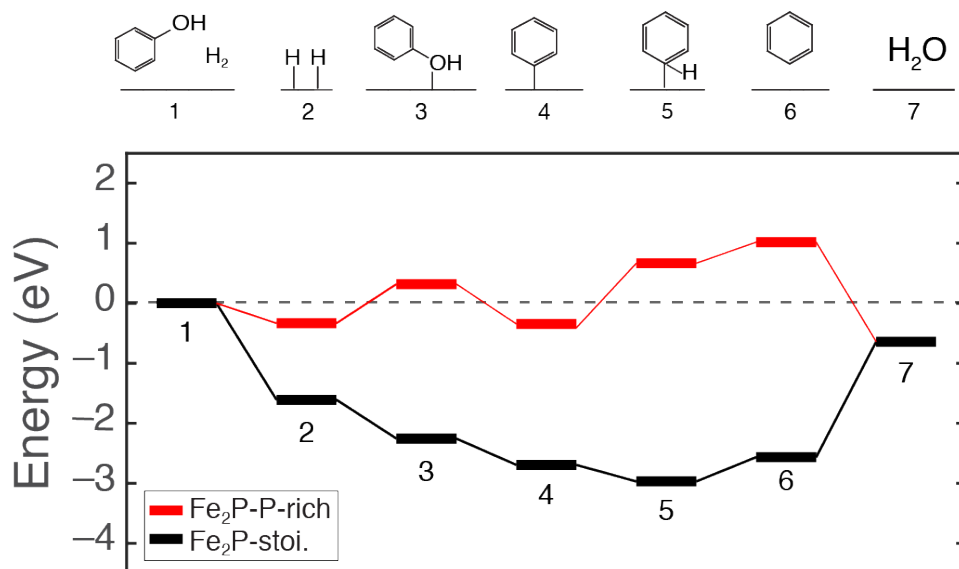

Figure S18: The direct reaction pathway of phenol deoxygenation on P-rich and stoichiometric surface of Fe_2P. The highly endothermic phenol adsorption energy over P-rich surface suggested an ensemble effect. The aggressive reduction of the ability to cleave C–O bond over P-rich Fe_2P indicated that the surface is less favorable for phenol deoxygenation than the "as-prepared" Fe_2P surface.

21
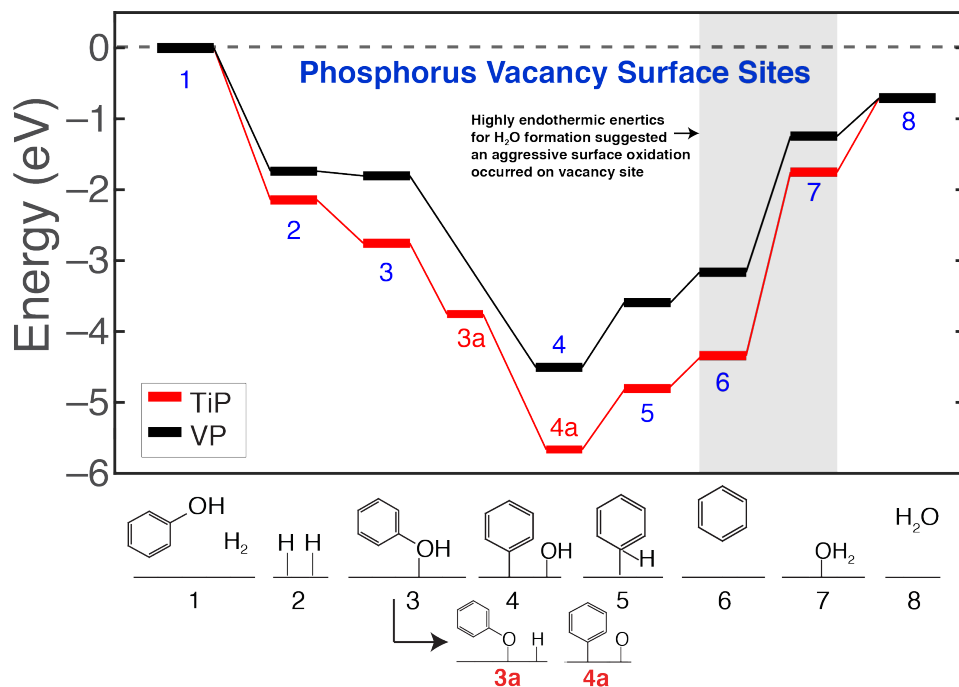
Figure S19: Deoxygenation reaction of phenol on the phosphorous vacancy reaction site of TiP and VP. The highly endothermic energetics for hydrogenation and water formation steps would likely result in catalytically inactive surfaces and poisoning.
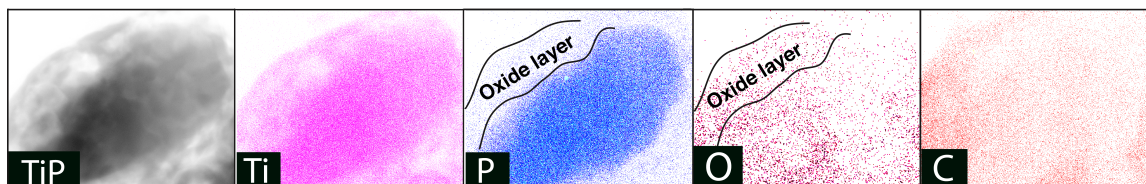
Figure S20: EDS analysis over TiP after guaiacol deoxygenation reaction showed a loss of phosphorus atoms and a significantly thick oxide layer indicating a lack of stability and a driving force for oxidation was present (noted in figure).
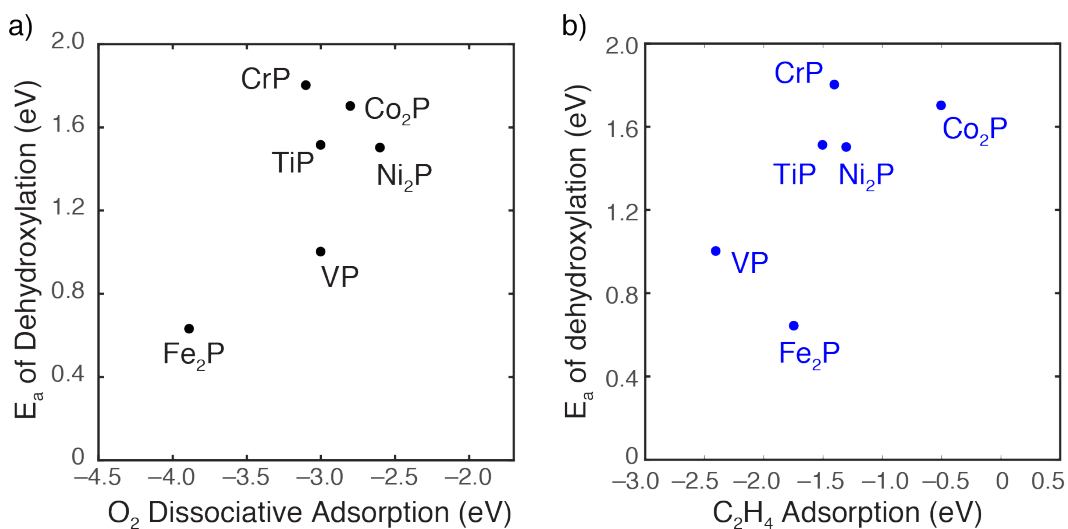
Figure S21: Scaling relationships of the reaction step energetics of dehydroxylation with the surface affinities of oxygen and carbon showing a lack of correlation. The energetics associated with electron density transfer during and after the C–O cleavage step is a likely source of this lack of correlation.
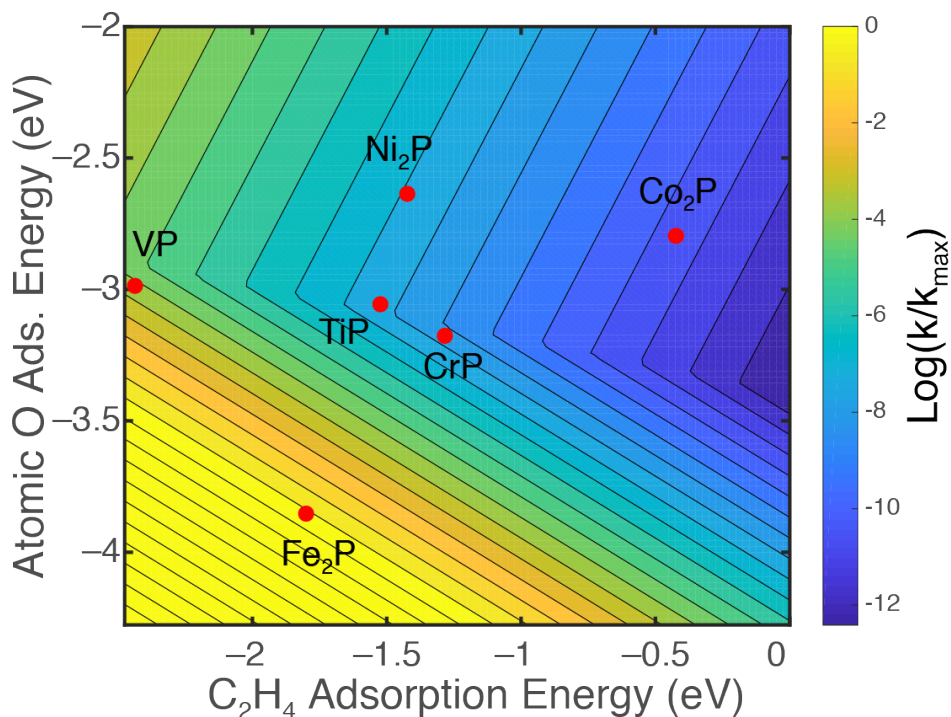
Figure S22: Correlation of the relative activity for C–O cleavage with C_2H_4 adsorption and dissociative O_2 adsorption showed a lack of correlation. As discussed in the text, this lack of correlation may be attributed to reduction and oxidation energetics as the C–O bond is cleaved, which are a function of effective electronegativity of the phosphide, bulk metal-to-nonmetal stoichiometry, and surface reaction site composition.

23
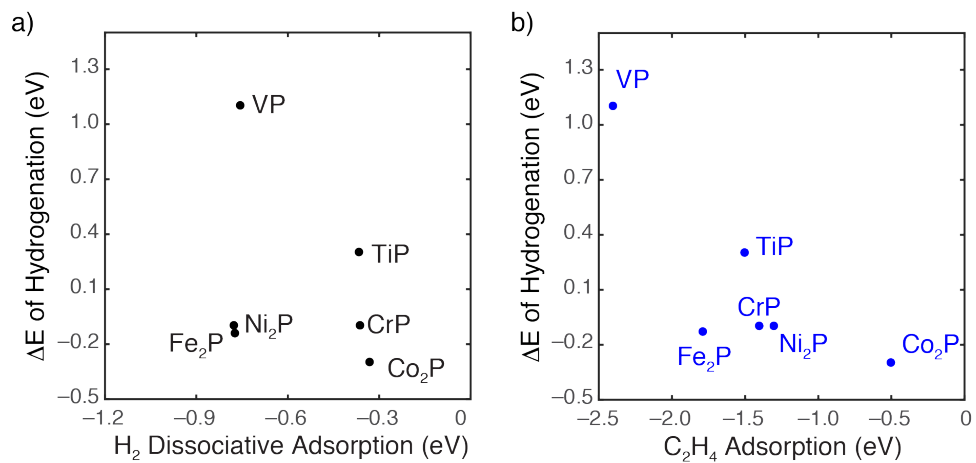
Figure S23: Correlations of the thermodynamic driving force for the hydrogenation step towards benzene formation with a) H_2 dissociative and b)C_2H_4 adsorption energies showing both surface reactivity markers play significant role in the reaction step energetics.
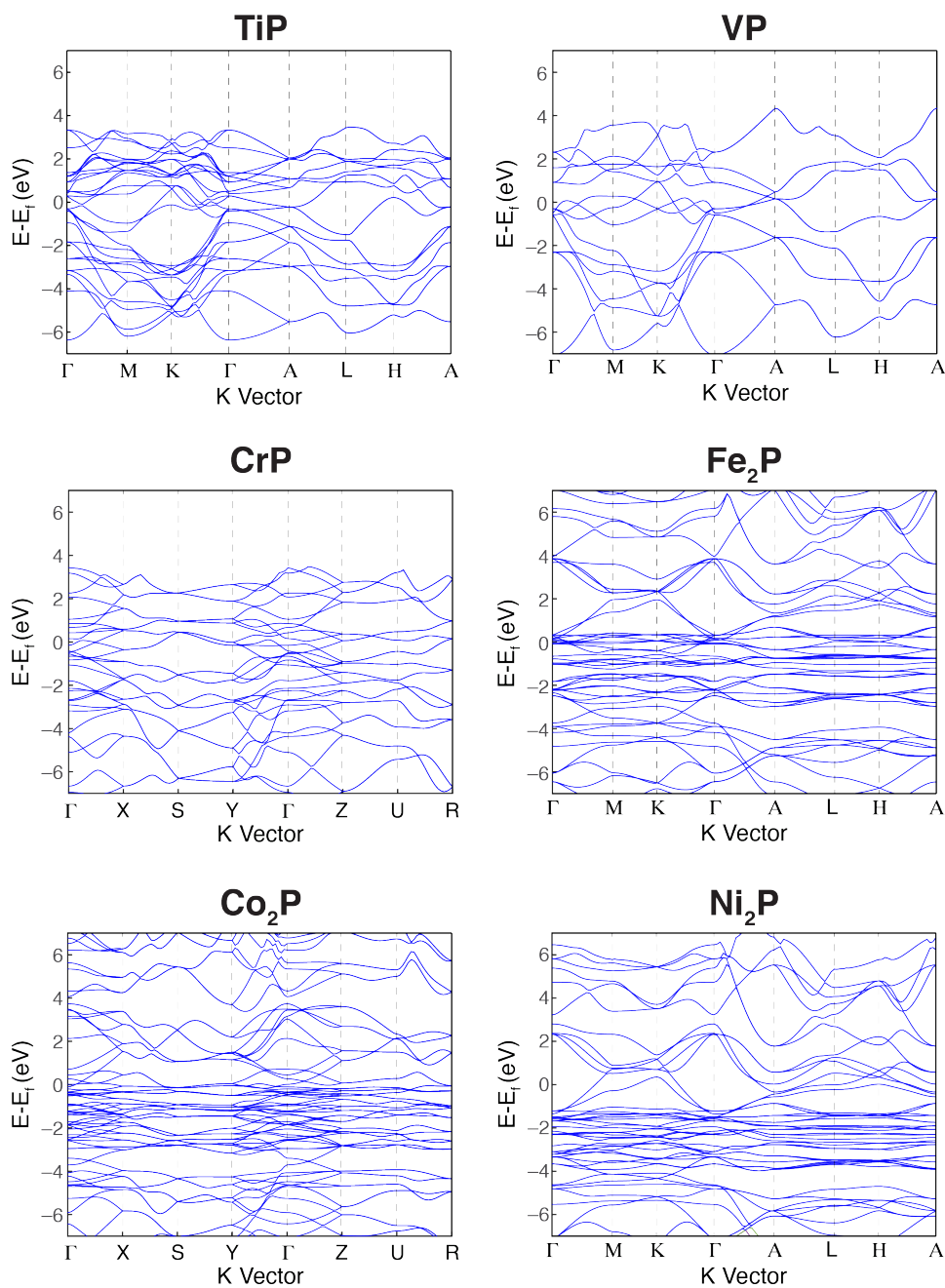
Figure S24: Correlations of the thermodynamic driving force for the hydrogenation step towards benzene formation with a) H_2 dissociative and b)C_2H_4 adsorption energies showing both surface reactivity markers play significant role in the reaction step energetics.

Table S1: Thermodynamic energetics for direct phenol deoxygenation towards benzene via utilizing the exchange and correlation functionals of PBE and PBEsol over the 1st row TM phosphides showing that this two functionals are comparable.

| Catalyst	E_{ads} of H_2 (eV)		E_{ads} of Phenol (eV)		Dehydroxylation (eV)		Hydrogenation (eV)		Ben. desorp. (eV)	
	PBEsol	PBE	PBEsol	PBE	PBEsol	PBE	PBEsol	PBE	PBEsol	PBE
TiP	−0.7	−0.6	−0.1	+0.1	−0.9	−0.8	+0.3	+0.2	+0.2	0.0
VP	−1.5	−1.3	−0.2	−0.1	−1.7	−1.4	+1.1	+0.7	+0.2	+0.1
CrP	−0.7	−0.4	−0.5	−0.1	−1.0	−0.9	−0.1	−0.3	+0.2	−0.1
Fe$_2$P	−2.1	−1.7	−0.5	−0.3	−1.4	−1.2	+0.5	+0.5	+0.3	−0.2
Co$_2$P	−0.7	−0.5	−0.1	0.0	−0.7	−0.5	−0.3	−0.7	+0.1	−0.1
Ni$_2$P	−1.6	−1.3	−0.4	−0.2	−0.4	−0.2	−0.1	−0.3	+0.4	+0.1

Table S2: Thermodynamic energetics for direct phenol deoxygenation towards benzene via utilizing the k-point mesh of 2x2x1 and 5x5x1 over the TiP showing that the results are identical.

	E_{dis} of H_2	E_{ads} of Phenol (eV)	Dehydroxylation (eV)	Hydrogenation (eV)	Ben. Desorp. (eV)
KPOINTS 2X2X1	−0.7	−0.1	−0.9	+0.3	+0.2
KPOINTS 5X5X1	−0.7	−0.1	−1.0	+0.2	+0.2

Table S3: Lattice information of the first row TM phosphides. Theoretical and experimental lattice parameters are coincided each other.

Catalyst	Space group	Theoretical (Å)			Experimental (Å)				Error (%)		
		a	b	c	a	b	c	Ref.	a	b	c
TiP	P 63/m m c	3.50	3.50	11.70	3.50	3.50	11.70	[14]	0	0	0
VP	P 63/m m c	3.15	3.15	6.24	3.18	3.18	6.22	[15]	0.9	0.9	-0.2
CrP	P n m a	5.25	3.05	5.89	5.35	3.11	6.00	[16]	1.8	1.7	1.8
Fe_2P	P -6 2 m	5.75	5.75	3.39	5.88	5.88	3.48	[17]	2.1	2.1	2.5
Co_2P	P n m a	5.54	3.44	6.47	5.65	3.51	6.61	[18]	2.0	2.0	2.0
Ni_2P	P -6 2 m	5.80	5.80	3.35	5.86	5.86	3.38	[19]	1.0	1.0	0.6

Table S4: Comparison of kinetic barriers of oxygen removal step via direct and indirect-a reaction pathway.

Catalyst	E_a of Direct dehydrogenaiton	E_a of Oxygen removal after dehydrogenation
TiP	1.70	**1.50**
VP	**1.02**	1.32
CrP	**1.73**	2.42
Fe_2P	**0.65**	1.33
Co_2P	**1.72**	1.80
Ni_2P	**1.50**	1.85

Table S5: Thermodynamic energetics for H_2O formation and desorption steps.

Catalyst	H_2O Formation (eV)	H_2O Desorption (eV)
TiP	+0.39	+0.06
VP	+1.28	+0.08
CrP	+0.56	+0.87
Fe_2P	+1.02	+0.55
Co_2P	+0.41	+0.44
Ni_2P	+0.81	+0.45

Table S6: Bader charge analysis of the oxygen and carbon of the dehydroxylation step fragments post C–O cleavage to ascertain the degree of electron transfer, which may contribute to reaction energetics. The superscript label of 'a' represents that there is just atomic O bond on TiP because of its indirect-a pathway (see Figure S9).

Catalyst	Charge of O in –OH	Charge of C in phenyl fragment
TiP	−1.9	−1.4
VP	−2.1	−1.4
CrP	−1.6	−1.3
Fe_2P	−1.6	−0.2
Co_2P	−2.1	−1.4
Ni_2P	−1.6	−0.3

Table S7: Bader charge analysis of the surface and bulk metal and phosphorus atoms to indicate the degree of polarization in the solid and at its surface. An insufficient number of FFT points in real space contributes to the charge balance error found in the calculations.

Catalyst	Surface		Bulk	
	Metal	Phosphorus	Metal	Phosphorus
TiP	+2.0	−1.2	+1.9	−2.1
VP	+1.6	−0.9	+1.6	−1.6
CrP	+1.2	−0.9	+1.2	−1.2
Fe_2P	+0.4	−0.8	+0.4	−0.9
Co_2P	+0.3	−0.4	+0.3	−0.5
Ni_2P	+0.2	−0.3	+0.2	−0.5

Table S8: Bond lengths between adsorbate and surface for each reaction step..

Catalyst	H_2 Disso. (Å)	Phenol Ads. (Å)	Dehydroxylation (Å)		Hydrogenation (Å)		Ben. formation (Å)
	–H*	phenol*	phenyl*	O*–H	phenyl*	–H*	benzene*
TiP	1.42	2.55	1.81	1.63	1.82	1.43	2.96
VP	1.43	2.44	1.81	1.62	1.81	1.43	2.03
CrP	1.44	2.24	1.82	1.93	1.81	1.43	2.03
Fe_2P	1.72	2.12	1.96	1.95	1.95	1.68	2.32
Co_2P	1.43	2.99	1.83	1.63	1.83	1.58	3.04
Ni_2P	1.79	2.09	1.94	1.99	1.93	1.78	2.24

Table S9: Bond lengths of C–OH and C–H for dehydroxylation and hydrogenation steps in their respective transition states.

Catalyst	Dehydroxylation (Å)	Hydrogenation (Å)
TiP	1.54	1.58
VP	1.63	1.46
CrP	1.75	1.59
Fe_2P	1.53	1.97
Co_2P	1.61	1.57
Ni_2P	1.78	1.70

3   INCAR for Dimer calculations

NWRITE = 2

ISTART = 0

GGA = PS

NPAR = 16

ENCUT = 400.0

EDIFF = 1E-7

LREAL = Auto

NELM = 60

NELMIN = 6

EDIFFG = -0.001

IBRION = 3

NSW = 3000

NBLOCK = 1

ALGO = FAST

ISMEAR = 0

SIGMA = 0.05

POTIM = 0.0

IDIPOL = 3

LDIPOL = .TRUE.

ICHAIN = 2

DdR = 0.005

DRotMax = 2

DFNMin = 0.01

DFNMax = 1.0

IOPT = 3

4   INCAR for NEB calculations

NWRITE = 2

ISTART = 0

ISPIN = 2

GGA = PS

NPAR = 16

NUPDOWN = 0

Electronic Relaxation

ENCUT = 400.0

EDIFF = 0.0001

LREAL = Auto

NELM = 60

NELMIN = 6

ALGO = FAST

Ionic relaxation

EDIFFG = -0.1

IBRION = 3

IOPT = 3

NSW = 3000

NBLOCK = 1

DOS related values

ISMEAR = 0

SIGMA = 0.05

POTIM = 0.0

Dipole corrections

IDIPOL = 3

LDIPOL = .TRUE.

ICHAIN = 0

IMAGES = 5

SPRING = -6

LCLIMB = .TRUE.

References

(1) Blanksby, S. J.; Ellison, G. B. *Acc. Chem. Res* **2003**, *36*, 255–263.

(2) Kästner, J.; Sherwood, P. *J. Chem. Phys.* **2008**, *128*, 014106.

(3) Xiao, P.; Sheppard, D.; Rogal, J.; Henkelman, G. *J. Chem. Phys.* **2014**, *140*, 174104.

(4) Henkelman, G.; Jónsson, H. *J. Chem. Phys.* **2000**, *113*, 9978.

(5) Heyden, A.; Bell, A. T.; Keil, F. J. *J. Chem. Phys.* **2005**, *123*, 224101.

(6) Sheppard, D.; Xiao, P.; Chemelewski, W.; Johnson, D. D.; Henkelman, G. *J. Chem. Phys.* **2012**, *136*, 074103.

(7) Liu, P.; Rodriguez, J. A.; Asakura, T.; Gomes, J.; Nakamura, K. *J. Phys. Chem. B* **2005**, *109*, 4575–4583.

(8) Moon, J.; Kim, E.; Lee, Y. *J. Catal.* **2014**, *311*, 144–152.

(9) Popczun, E. J.; McKone, J. R.; Read, C. G.; Biacchi, A. J.; Wiltrout, A. M.; Lewis, N. S.; Schaak, R. E. *J. Am. Chem. Soc.* **2013**, *135*, 9267–9270.

(10) Wang, X.; Wan, F.; Gao, Y.; Liu, J.; Jiang, K. *J. Cryst. Growth* **2008**, *310*, 2569–2574.

(11) Muthuswamy, E.; Savithra, G. H. L.; Brock, S. L. *ACS Nano* **2011**, *5*, 2402–2411.

(12) Carenco, S.; Resa, I.; Le Goff, X.; Le Floch, P.; Mézailles, N. *Chem. Commun.* **2008**, 2568.

(13) Government, U. *National Institute of Standards and Technology* **http://webbook.nist.gov, 2009**,

(14) Lundström, T.; Snell, P.-O.; Rasmussen, S. E.; Holmberg, P.; Eriksson, G.; Blinc, R.; Paušak, S.; Ehrenberg, L.; Dumanović, J. *Acta Chemica Scandinavica* **1967**, *21*, 1343–1352.

(15) Selte, K.; Kjekshus, A.; Andresen, A. *Acta Chemica Scandinavica* **1972**, *26*, 4057–4062.

(16) Selte, K.; Kjekshus, A.; Andresen, A. F. *Acta Chemica Scandinavica* **1972**, *26*, 4188–4190.

(17) Zvada, S.; Medvedeva, L.; Sivachenko, A.; Khartsev, S. *J. Magn. Magn. Mater.* **1988**, *72*, 349–356.

(18) Fruchart, R.; Roger, A.; Senateur, J. P. *J. Appl. Phys.* **1969**, *40*, 1250–1257.

(19) Rundqvist, S. *Acta Chemica Scandinavica* **1962**, *16*, 992–998.